Journal of Magnetic Resonance 204 (2010) 99–110

Contents lists available at ScienceDirect

Journal of Magnetic Resonance

journal homepage: www.elsevier.com/locate/jmr

Two-dimensional MAS NMR correlation protocols involving double-quantum filtering of quadrupolar spin-pairs

Mattias Edén

Physical Chemistry Division, Department of Materials and Environmental Chemistry, Arrhenius Laboratory, Stockholm University, SE-106 91 Stockholm, Sweden

ARTICLE INFO

Article history:
Received 22 November 2009
Revised 7 February 2010
Available online 12 February 2010

Keywords:
Dipolar recoupling
Double-quantum coherence
Homonuclear correlation spectroscopy
Multiple-quantum filtration
Internuclear proximities
Quadrupolar tensor orientations
Half-integer spin quadrupolar nuclei
Sillimanite

ABSTRACT

Three two-dimensional (2D) NMR homonuclear correlation techniques invoking double-quantum (2Q) filtration of the central transitions of half-integer spins are evaluated numerically and experimentally. They correlate directly detected single-quantum (1Q) coherences in the t_2 domain with either of 1Q, two-spin 2Q or single-spin multiple-quantum coherence-evolutions in the indirect (t_1) dimension. We employ experimental ^{23}Na and ^{27}Al NMR on sodium sulfite and the natural mineral sillimanite ($SiAl_2O_5$), in conjunction with simulated 2D spectra from pairs of dipolar-recoupled spins-3/2 and 5/2 at different external magnetic fields, to compare the correlation strategies from the viewpoints of 2D spectral resolution, signal sensitivity, implementational aspects and their relative merits for establishing internuclear proximities and quadrupolar tensor orientations.

1. Introduction

1.1. Background

There is a growing interest in designing and using techniques to correlate NMR interaction parameters under magic-angle spinning (MAS) conditions, where at least one of the participating nuclei possesses half-integer spin [1,2]. A subset of this wide family of solid state NMR methodologies targets the exploration of internuclear proximities/connectivities between quadrupolar nuclei of the same species in inorganic materials: the homonuclear correlations are established via spin–spin interactions mediated either through space or chemical bonds. Recent reviews are given in [1,3].

Fig. 1 depicts three distinct 2D NMR protocols for correlating the signals from quadrupolar nuclei in close spatial proximity. They incorporate a pulse-block for exciting two-spin double-quantum coherences (2QC) between the central transitions (CTs) in a pair of dipolar-(re)coupled half-integer spins; such coherences are henceforth abbreviated "$2Q_{CT}$". The MAS-diminished dipolar interactions may partially be restored by using rf pulse sequences conforming to the R-symmetry class [4–7], as described in detail in our previous work on 2Q-recoupling of quadrupolar nuclei [8–10]. In the numerical and experimental demonstrations herein, we employ either of the $R2_2^1R2_2^{-1}$ [8] or $R2_4^1R2_4^{-1}$ [9] recoupling schemes. In both cases, the spin-S CT nutation frequency $\omega_{nut}^{CT} = (S+1/2)\,|\,\gamma_S\,|\,B_1$ obeys $\omega_{nut}^{CT} = \omega_r/2$ during recoupling, where γ_S is the spin magnetogyric ratio, B_1 the rf amplitude, $\omega_r = 2\pi/\tau_r$ the angular rotation frequency of the sample and τ_r its rotational period. When sandwiched between two CT-selective $\pi/2$-pulses, the recoupling pulse sequences generate approximately an effective 2Q dipolar Hamiltonian involving CT spin-operators $S_j^{\pm}S_k^{\pm}$ multiplied by a scaled through-space dipolar coupling constant b^{jk} between the homonuclear spins j and k [8–10].

1.2. 2Q–1Q correlation scheme

A double-quantum filtering (2QF) procedure involves the excitation of $2Q_{CT}$ from z-magnetization for an interval τ_{exc} [11,12]. The reverse process, labeled by "$2Q_{CT} \rightarrow Z$" in Fig. 1, is performed by repeating the same pulse train for τ_{rec}, but phase-shifting all rf pulses (including the bracketing pulses) by $\pi/2$. The 2QC excitation and reconversion intervals need not necessarily be equal [5,13]. The NMR signals are detected after a subsequent Z-filter interval (τ_Z) and a $\pi/2$ read pulse. As distinct types of MQC may exist in half-integer spin systems, either involving a single spin or a pair of spins, we denote the 2QF process of the CTs of *spin-pairs* by "$2QF_{CT}$" (see Fig. 1). The fraction of initial longitudinal CT magnetization recovered after the $2QF_{CT}$ event is denoted $f_{Z\rightarrow Z}^{2QF}$ and referred to as the 2QF efficiency. The 2QF scheme used herein only differs from the traditional spin-1/2 procedure [11,12] in two respects: (i) a CT-selective π-pulse is inserted between the $2Q_{CT}$ excitation and reconversion events [14]. It is phase-cycled to retain

E-mail address: mattias.eden@mmk.su.se

1090-7807/$ - see front matter © 2010 Elsevier Inc. All rights reserved.
doi:10.1016/j.jmr.2010.02.007

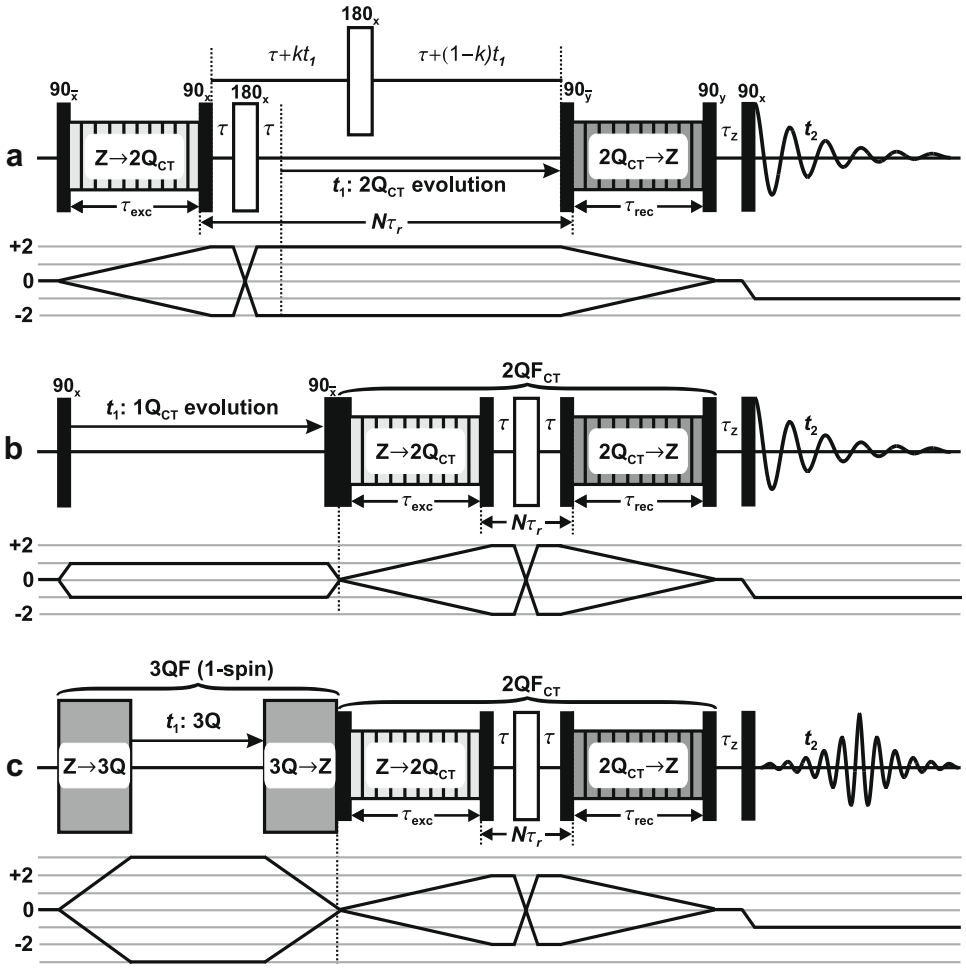

Fig. 1. (a) 2Q–1Q, (b) 1Q–1Q[2QF] and (c) 3Q–1Q[2QF] 2D NMR correlation protocols employing $2QF_{CT}$ for probing proximities between half-integer quadrupolar spins, with their corresponding coherence-transfer pathways [40] shown beneath. Phase-cycle implementations that simultaneously allow all desired coherence transfers but reject all undesirable ones are given in Ref. [10] for the experiment in (a) and in the SI for those of (b) and (c). The upper part of (a) depicts an alternative t_1-sampling approach [14] (discussed in Section 3.2). Symmetry-based $R2_2^1R2_2^{-1}$ or $R2_4^1R2_4^{-1}$ 2Q-recoupling schemes are utilized for $2QF_{CT}$ [8–10]. They are sandwiched between two CT-selective 90°-pulses (illustrated throughout by black rectangles) of opposite rf-phases. Each rf pulse flip-angle is given in degrees, with the corresponding rf phase specified as the direction of the rf field vector along a rotating-frame axis (subscripts $x, y, \bar{x}, \bar{y}$). All rf pulses in (a–c) are CT-selective, except for those driving the Z → 3Q and 3Q → Z transfers in (c).

exclusively the $\pm 2Q_{CT} \rightarrow \mp 2Q_{CT}$ pathways to block 2QC from the satellite transitions (STs). (ii) As the 2Q-recoupling schemes $R2_2^1R2_2^{-1}$ and $R2_4^1R2_4^{-1}$ lack the γ-encoding property [12], two delays τ are inserted to arrange a total time-span of an even multiple of rotational periods ($N\tau_r$) between the as-indicated time-points in each of Fig. 1(a–c) [8].

By introducing a "t_1" time interval incremented in steps of τ_r, the $2QF_{CT}$ scheme converts into a 2Q–1Q correlation NMR experiment, as first demonstrated for half-integer spins by Painter and Duer [15]. The basic implementation of Fig. 1(a) was presented by Mali and co-workers [14]. 2D Fourier transformation of the recorded data-set $s(t_1, t_2)$ yields a 2D NMR spectrum that correlates the indirectly detected $2Q_{CT}$ frequencies $\omega_{jk} = \omega_j + \omega_k$ (vertical dimension; ω_1 coordinate) with their $1Q_{CT}$ frequency components ω_j and ω_k (ω_2 coordinate).

Here we present two alternative homonuclear 2D NMR correlation techniques for quadrupolar spins—both invoking $2QF_{CT}$ events, but differing in the coherence orders evolved during t_1—and compare their relative merits and limitations with the 2Q–1Q scheme. As opposed to the latter, the $2QF_{CT}$ stage is appended to intervals of $1Q_{CT}$ or multiple-quantum coherence (MQC) evolution, as depicted in Fig. 1(b) and (c), respectively. Throughout, reference to "MQC" in the absence of a subscript "CT" implies a *single-spin* MQC.

1.3. 1Q–1Q 2QF correlation scheme

The rf pulse diagram of Fig. 1(b) correlates $1Q_{CT}$ frequencies in the indirect 2D spectral dimension with those of $2QF_{CT}$ $1Q_{CT}$ frequencies in the direct dimension. It will onwards be referred to as a 1Q–1Q[2QF] NMR experiment and constitutes the quadrupolar-spin analog of existing spin-1/2 solid state NMR correlation techniques incorporating a *M*QF "mixing" stage, as previously demonstrated for $M = 2$ [16] or $M = 3$ [17] quantum coherences. Close spatial *j*–*k* proximities are revealed as "cross-peaks" appearing at a frequency combination $(\omega_1, \omega_2) = (\omega_j, \omega_k)$ in the 2D NMR spectrum, meaning that the t_2-detected $2QF_{CT}$ signal of spin *k* originated from the t_1-evolution of spin *j*. Refs. [3,16,18] highlight the advantages of 2Q–1Q correlation experiments relative to 1Q–1Q ones that invoke magnetization transfers during mixing [19–23]: the $2QF_{CT}$ stage of 2Q–1Q and 1Q–1Q[2QF] NMR acquisitions removes all signals associated with isolated spins and equalizes the detected signal amplitudes of spins *j* and *k*, in contrast with experiments exploiting direct magnetization transfers [19–23]. Hence, a 1Q–1Q[2QF] experiment emphasizes the desirable NMR signals that reflect internuclear proximities and reduces t_1-noise associated with the largest (but uninformative) NMR peaks stemming from non-exchanged magnetization in 1Q–1Q 2D spectra [16,18].

Nevertheless, as for magnetization–exchange processes, unambiguous detection of $j \leftrightarrow j$ and $k \leftrightarrow k$ auto-correlations is precluded by the unavoidable emergence of undesirable (ω_j, ω_j) and (ω_k, ω_k) diagonal peaks in a 1Q–1Q[2QF] NMR spectrum for each $j \leftrightarrow k$ correlation [16,18]. This represents the main disadvantage with using contracted 2Q excitation and reconversion events [Fig. 1(b)] instead of arranging a t_1-dependent $2Q_{CT}$ frequency-encoding as in the 2Q–1Q protocol of Fig. 1(a).

1.4. MQ–1Q 2QF correlation scheme

Compared to 1Q–1Q[2QF] NMR spectra, enhanced frequency-dispersion of the peaks appearing along the indirect spectral dimension is generally obtained by combining a spin-pair filter with a MQ–1Q correlation experiment of half-integer spins; the latter is commonly referred to as multiple-quantum MAS (MQMAS) [24–26]. The resulting protocol is labeled MQ–1Q[2QF] and its 3Q version is depicted in Fig. 1(c). The gray rectangular blocks sandwiching the t_1-interval represents a 3Q filter (3QF) addressing *individual* quadrupolar spins. Several options exist for implementing such coherence transfers [25,27–37]. The $2QF_{CT}$ stage is naturally introduced after the MQ → Z conversion in a *Z*-filter MQMAS experiment [38,39], as in previous 2D schemes incorporating a mixing period for driving magnetization exchange [19–23]. The present 3Q–1Q[2QF] pulse scheme is formed by replacing the mixing pulses in the 3Q–1Q correlation technique of Ref. [23] by a $2QF_{CT}$ segment.

In general, a high-resolution ("isotropic") dimension is obtained by subjecting the acquired MQMAS 2D data-set to a shear transformation [24,25,40]. This operation may be viewed as a rotation of the second-order quadrupolar-broadened ridge such that it becomes aligned with the ω_2 spectral axis. The ω_1-projection of the sheared 2D spectrum then displays one narrow peak per quadrupolar site in the structure, provided that the latter is perfectly ordered. However, active magnetization exchange (or a $2QF_{CT}$ process, as in the present context) subsequent to the MQC-evolution introduces broad signal components along the "isotropic" dimension: shearing then usually do not help the identification of correlation signals and will not be used in the processing of the MQ–1Q[2QF] spectra presented herein.

In the following, we provide a comprehensive comparison of the various 2D NMR correlation experiments from the viewpoints of signal sensitivity, spectral resolution and their relative merits in revealing internuclear proximities/connectivities. This is addressed primarily by numerically simulated 2D NMR spectra from pairs of $S = 3/2$ and 5/2, using different external magnetic fields (9.4 T, 14.1 T and 18.8 T), chemical shift-differences and relative orientations of the electric-field-gradient (efg, here called "quadrupolar") tensor orientations. The quadrupolar tensor is characterized by a quadrupolar coupling constant $C_Q = e^2qQ/h$ and an asymmetry parameter $\eta = (V_{yy} - V_{xx})/V_{zz}$, where $\{V_{ij}\}$ denote its principal values. Tensor orientations are described by Euler angles $\Omega_\Lambda = \{\alpha_\Lambda, \beta_\Lambda, \gamma_\Lambda\}$ [41], where Λ represents either the quadrupolar (Q) or dipolar (DD) interaction. Experimental results are provided by ^{23}Na ($S = 3/2$) NMR on Na_2SO_3 and ^{27}Al ($S = 5/2$) NMR on the mineral sillimanite, $SiAl_2O_5$.

2. Results for $S = 3/2$

2.1. Experiments: Na_2SO_3

An experimental demonstration of a 3Q–1Q[2QF] ^{23}Na NMR spectrum is shown in Fig. 2. It was acquired from a powder of Na_2SO_3 at 9.4 T. Sodium sulfite comprises three distinct ^{23}Na sites, labeled **1**, **2** and **3** and populated as 1:1:2. NMR parameters of

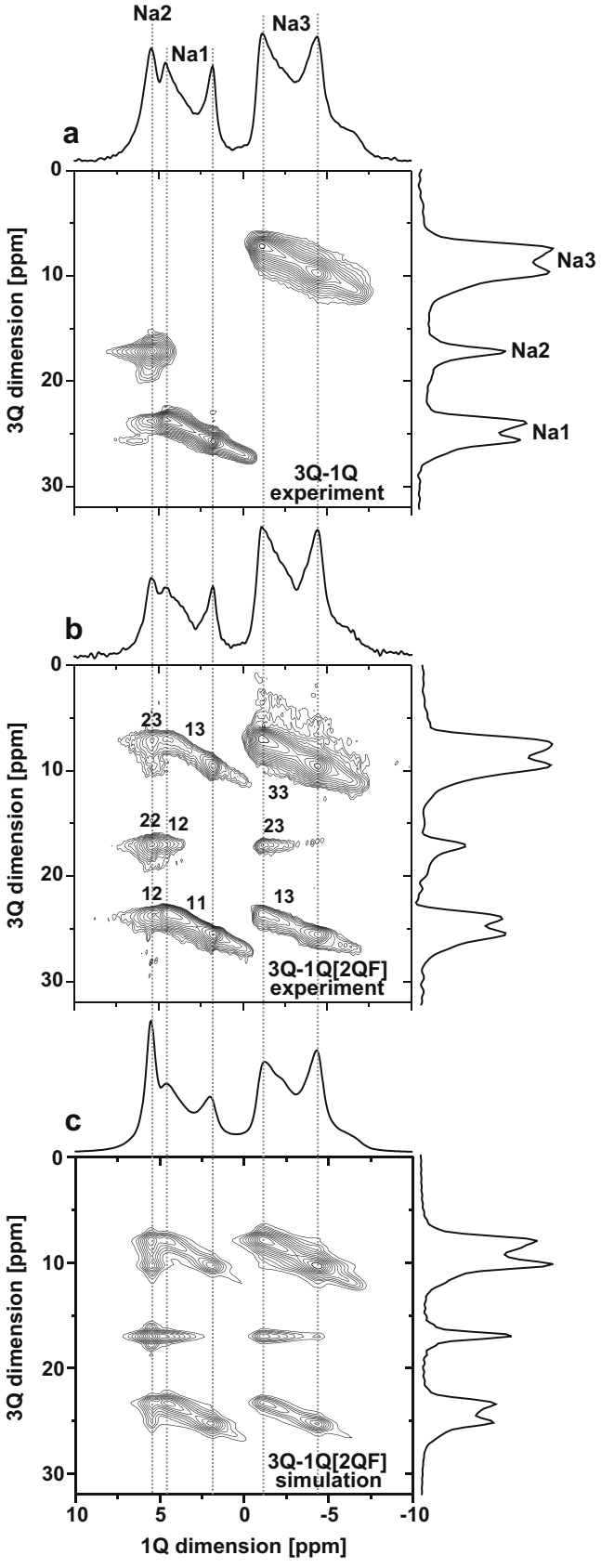

Fig. 2. Experimental 3Q–1Q[2QF] ^{23}Na NMR results from Na_2SO_3 undergoing 12.0 kHz MAS at $B_0 = 9.4$ T. The 2D spectra were recorded by the pulse scheme of Fig. 1(c) in the absence (a) and presence (b) of $2QF_{CT}$. The NMR signals of the three distinct ^{23}Na sites are identified by Na**1**, Na**2** and Na**3** in the projections displayed in (a). Each $2QC_{CT}(^{23}Naj—^{23}Nak)$ signal is assigned as jk ($j, k = \mathbf{1}, \mathbf{2}, \mathbf{3}$) in (b). (c) Calculated 3Q–1Q[2QF] NMR spectrum (see Section 6).

Na_2SO_3 were first reported by Power [42]; here we use the slightly modified values of Ref. [43]. All quadrupolar tensors are axially symmetric ($\eta = 0$). ^{23}Na**1** and ^{23}Na**3** have almost equal quadrupolar coupling constants $C_Q \approx 1.1$ MHz, whereas that of ^{23}Na**2** is very small (≈ 0.15 MHz). The isotropic chemical shifts for sites **1** and **2** are nearly coincident at 5.6 ppm, while that of ^{23}Na**3** is around zero. The closest homonuclear internuclear separation involves ^{23}Na**1**–^{23}Na**2** ($b^{jk}/2\pi = -286$ Hz), but there is a larger number of couplings among all other sites [43].

Fig. 2(a) displays an experimental 3QMAS spectrum of Na_2SO_3, which reveals three well-separated ^{23}Na NMR resonances. The result by appending a $2QF_{CT}$ stage is displayed in Fig. 2(b). The signal separation is overall better in the 3Q–1Q[2QF] spectrum compared to those of previous 2Q–1Q correlations recorded under similar experimental conditions; e.g., see Refs. [8,43]. Besides the ^{23}Naj—^{23}Naj ($j = \mathbf{1}, \mathbf{2}, \mathbf{3}$) signals, cross-peaks are visible between all distinct ^{23}Na sites for the employed value $\tau_{exc} = 667$ μs. The experiment is readily reproduced by the simulation in Fig. 2(c).

2.2. Simulations

Fig. 3 shows numerically exact simulations of (a–c) 1Q–1Q[2QF], (d–f) 2Q–1Q and (g–i) 3Q–1Q[2QF] correlation NMR powder spectra at increasing external magnetic fields. Two spins-3/2, labeled **1** and **2**, were assumed with NMR interaction parameters typical for ^{23}Na. ω_2-projections of the 1Q–1Q[2QF] spectra are displayed at the top of Fig. 3 (those of the other 2D schemes are very similar). The $2QF_{CT}$ second-order quadrupolar-broadened powder patterns of both sites (particularly #**2**) manifest distortions compared to the corresponding "ideal" 1D MAS peakshapes. The degree of spectral alterations depends on the particular dipolar recoupling method and its duration of application (τ_{exc}), the spectrometer carrier frequency relative to the NMR signal positions, as well as on the *orientations* of the interaction tensors involved. The left signal portion of the powder pattern is often enhanced compared to that of the right: for certain relative orientations of the quadrupolar and dipolar tensors, the low-ppm spectral region is almost extinguished, as discussed further in Section 5. As opposed to the narrow signal ridges deriving from the ^{23}Na–^{23}Na pairs of Na_2SO_3 (Fig. 2), all 2D cross-peaks from the present spin-pair are relatively broad: this reflects non-coincident quadrupolar tensors.

For the given set of quadrupolar parameters and small isotropic chemical shift difference of $\Delta_{iso} = 5$ ppm, Fig. 3 shows that in the absence of 3QMAS experimentation, an external magnetic field of 18.8 T is required to completely separate the NMR signals from sites **1** and **2**. However, owing to the interplay between quadrupolar and chemical shifts, even 3QMAS fails to resolve the two signals at $B_0 = 9.4$ T [Fig. 3(g)]. Hence, *in this case*, 1Q–1Q[2QF] and 3Q–1Q[2QF] correlations provide comparable spectral resolution, meaning that the former and much more signal-sensitive experiment is preferred.

When focussing on the inter-spin proximity information provided by each correlation method, it should first be considered what information is *a priori* available. If it is known that there are *two* distinct quadrupolar sites, all 2D spectra in Figs. 3 and S1 (see Supporting Information, SI) unambiguously reveal the **1**–**2** proximities. However, if the precise number of sites is unknown, the 3Q–1Q[2QF] results at 14.1 T and 18.8 T would simultaneously provide the number of sites—through the presence of two diagonal peaks—as well as revealing the **1**–**2** spatial proximity. The same information is obtained from any 2D spectrum obtained at 18.8 T, but strictly not (unambiguously) from the rest of the 2D NMR spectra obtained for the parameters used in Fig. 3.

3. Results for $S = 5/2$

3.1. Simulations

All essential features of 2D correlation spectra recorded by the 2Q–1Q or 1Q–1Q[2QF] techniques are captured by the previous $S = 3/2$ simulations. The main consequence when considering half-integer spins $S > 3/2$, is a scaling of the second-order quadrupolar shifts and the accompanying peak-broadening by $\sim [2S(2S-1)]^{-1}$. Small chemical shift differences among the quadrupolar sites remains as the primary obstacle for identifying the various auto-correlation and cross peaks by $2QF_{CT}$-based 2D experiments.

For $S = 5/2$, however, the MQ–1Q[2QF] technique offers the possibility to perform either of $M = 3$ or $M = 5$ correlations: Fig. 4 focusses on comparing the resolution expected from 5Q–1Q[2QF] experiments relative to that of 3Q–1Q[2QF] ones by numerically calculated NMR spectra at $B_0 = 9.4$ T. The simulation parameters are representative for two distinct $^{27}AlO_6$ units in a network structure. The top panel of Fig. 4 illustrates the case of equal isotropic chemical shifts, meaning that the NMR signal-separation rests solely on the distinct isotropic quadrupolar shifts of sites **1** and **2**. Their 1QC NMR lineshapes display significant spectral overlap (see the 1D MAS NMR spectra in Fig. 5). The **1**–**1** and **2**–**2** auto-correlation peaks are separated from each other in the 3Q–1Q[2QF] NMR spectrum of Fig. 4(a), which is unfortunately not obvious due to severe overlap with their associated **1**–**2** cross-peaks. Hence, this constitutes yet another case where a 3Q–1Q[2QF] acquisition is not offering much improved spectral resolution compared to that of a 1Q–1Q[2QF] spectrum (e.g., see Fig. 3). However, Fig. 4(b) reveals a significant enhancement in the NMR signal separation by utilizing a 5Q–1Q[2QF] experiment as the two main groups of resonances from sites **1** and **2** are now well-resolved.

We next consider the same spin-pair, but introduce a chemical shift difference of $\Delta_{iso} = 10$ ppm ($\delta^1_{iso} = 10$ ppm; Fig. 4(c) and (d)). This provides a markedly enhanced resolution in the 3Q–1Q[2QF] spectrum, whereas that of the 5Q–1Q[2QF] experiment remains similar to the previous case. The bottom row of 2D spectra in Fig. 4 shows the result of keeping $\Delta_{iso} = 10$ ppm, but employing coinciding quadrupolar tensors.

3.2. Experiments: sillimanite

The mineral sillimanite represents one of the $SiAl_2O_5$ polymorphs. The structure is depicted in Fig. 6(a). It consists of chains of edge-sharing AlO_6 octahedra (along the *c*-axis) that cross-link chains of alternating $(Si,Al)O_4$ tetrahedra. The $SiO_4 : AlO_4 : AlO_6$ populations relate as 1:1:1 and the structure comprises directly connected AlO_4–AlO_6 and AlO_6–AlO_6 polyhedra. The ^{27}Al MAS NMR spectrum of Fig. 6(b) manifests two relatively broad powder NMR peakshapes, associated with C_Q-values of 6.7 MHz and 8.8 MHz for ^{27}Al in tetrahedral and octahedral coordination, respectively [44].

Table S1 summarizes the number of ^{27}Al–^{27}Al internuclear contacts over a radius of 5.2 Å. When simultaneously considering the sizes of coupling constants and the number of dipolar interactions, the strongest internuclear contacts are those between $^{27}AlO_4$–$^{27}AlO_6$ and $^{27}AlO_6$–$^{27}AlO_6$ polyhedra. Fig. 6(c) shows a 1Q–1Q[2QF] spectrum recorded by using one completed $R2^1_4R2^{-1}_4$ sequence for $2QF_{CT}$. The strong Al(IV)–Al(VI) contacts give clearly visible cross-peaks. The dominance of these connectivities are confirmed by the corresponding 2Q–1Q correlation spectrum in Fig. 6(d), which also reveals Al(IV) auto-correlations over Al–O–Si–O–Al motifs. This 2D ridge is emphasized visually due to its narrowness. The total ^{27}Al $2QF_{CT}$ efficiency was 2.7% and peak inte-

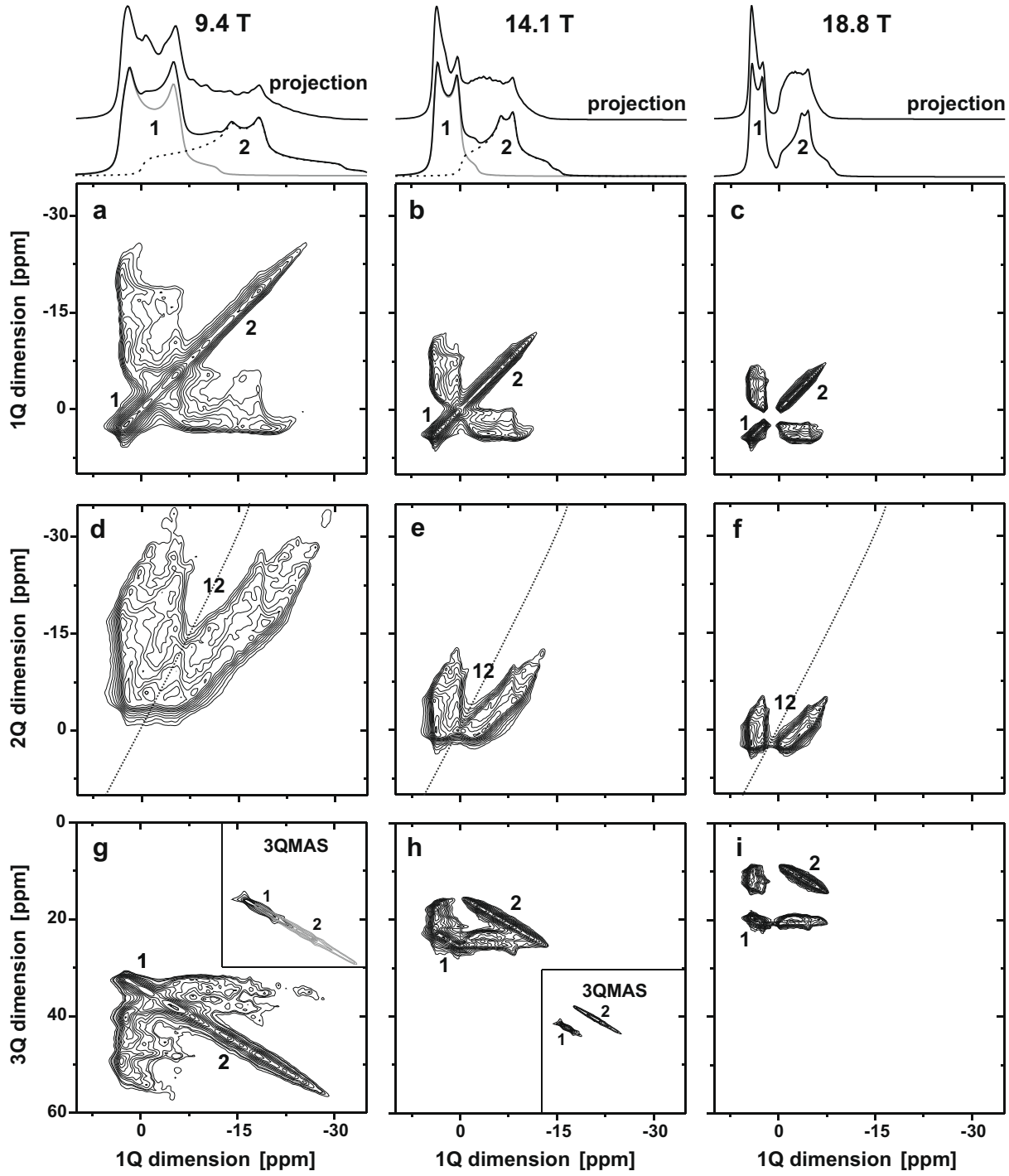

Fig. 3. Numerically simulated 1Q–1Q[2QF] (a–c), 2Q–1Q (d–f) and 3Q–1Q[2QF] (g–i) NMR spectra. The calculations assumed a powder of two coupled $S = 3/2$, labeled **1** and **2** and undergoing 20.0 kHz MAS at each of three distinct magnetic fields B_0 of 9.4 T (left column), 14.1 T (mid) and 18.8 T (right). The Larmor frequency of ^{23}Na was employed throughout. The top 1D NMR spectra represent the ω_2-projections of the 2D spectra in (a–c), shown together with calculated 1D MAS NMR spectra (using CT-selective pulses) and accompanying component peaks. "Auto-correlation" NMR peaks of sites **1** and **2** are indicated by the numbers shown in the top and bottom rows of spectra. The insets in (g,h) represent 3Q–1Q simulations obtained by omitting the $2QF_{CT}$ stage in Fig. 1(c). Note the different vertical scale used in (g–i) compared to (a–f). Parameters: $b^{12}/2\pi = -220$ Hz; $\{\delta^1_{iso}, \delta^2_{iso}\} = \{5, 0\}$ ppm; $\{C^1_Q, C^2_Q\} = \{1.75, 2.4\}$ MHz; $\{\eta^1, \eta^2\} = \{0.15, 0.75\}$; $\Omega^{12}_{DD} = (0, 0, 0)$; $\Omega^1_Q = (0, 90^\circ, 0)$; $\Omega^2_Q = (0, 90^\circ, 90^\circ)$.

grations gave the following approximative estimates of the correlation intensities: AlO_4—AlO_4 : $AlO_4 - AlO_6$: $AlO_6 - AlO_6 \approx 0.07 : 0.78 : 0.15$. The SI discusses possible reasons for the unexpectedly weak $2Q_{CT}(AlO_6$—$AlO_6)$ correlations.

For consistency, both 2D acquisitions of Fig. 6 used rotor-synchronized t_1-incrementation, despite that the 1Q–1Q[2QF] experiment allows for arbitrary sampling. The required span of $N\tau_r$ between the $2Q_{CT}$ excitation and reconversion events constitutes the primary drawback of the 2Q–1Q experiment compared to the other correlation strategies of Fig. 1. This restricts the t_1-sampling to avoid an undesirable spinning sideband formation along the indirect 2Q–1Q spectral dimension (see [8,14,45], for details). Ref. [14] introduced an approach to circumvent folding by splitting up the t_1 interval into kt_1 and $(1-k)t_1$ segments $(0 \leqslant k \leqslant 0.25)$ [see Fig. 1(a)]. This scales each $2Q_{CT}$ frequency by $(1-2k)$ [14], but has two disadvantages: (i) The spectral resolution in the

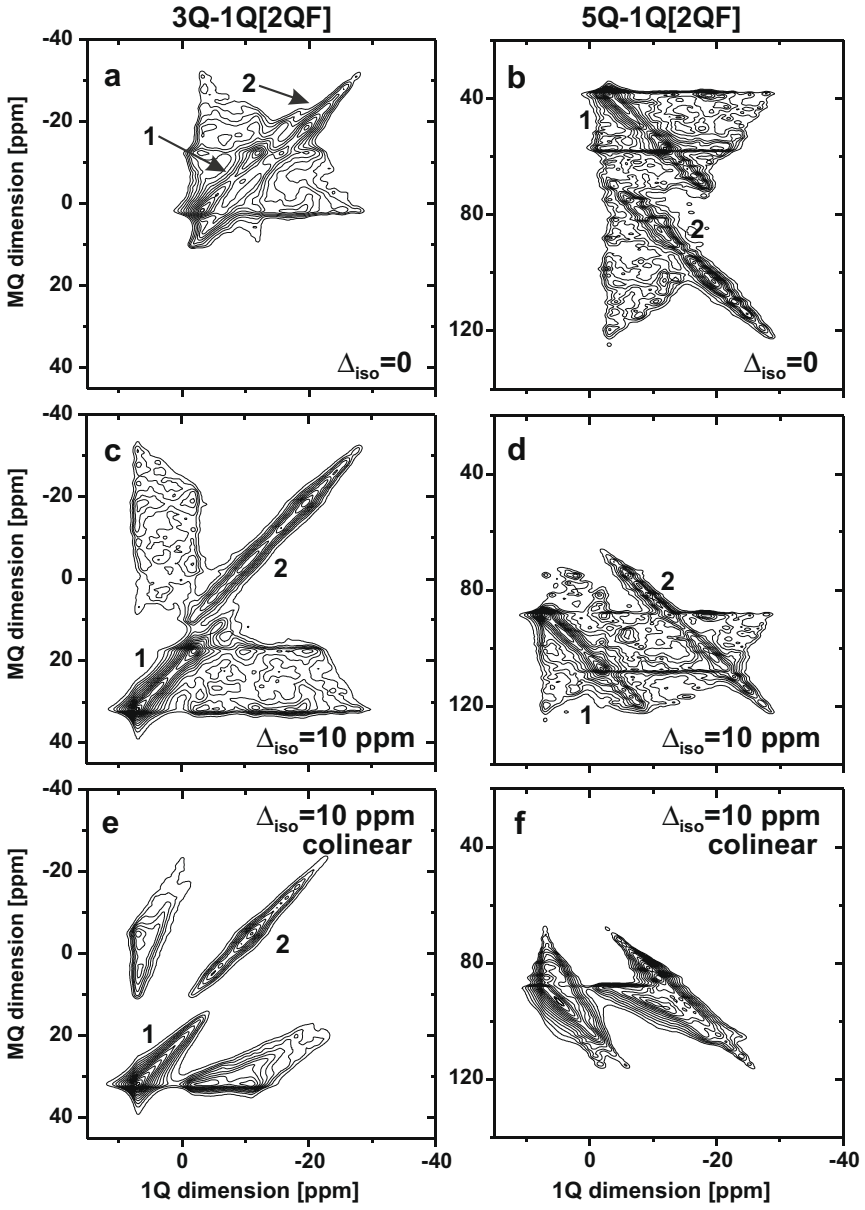

Fig. 4. Numerically simulated 3Q–1Q[2QF] (left panel) and 5Q–1Q[2QF] (right panel) spectra of $S = 5/2$ spin-pairs at $B_0 = 9.4$ T and $\omega_r/2\pi = 20.0$ kHz. A Larmor frequency of ^{27}Al ($\omega_0/2\pi = -104.288$ MHz) was assumed for the two spins **1** and **2**, together with the following parameters: $b^{12}/2\pi = -100$ Hz; $\{C_Q^1, C_Q^2\} = \{3.75, 5.0\}$ MHz; $\{\eta^1, \eta^2\} = \{0, 0.50\}$; $\Omega_{DD}^{12} = (0, 0, 0)$. Isotropic chemical shifts were varied as (a, b) $\{\delta_{iso}^1, \delta_{iso}^2\} = \{0, 0\}$ ppm and (c–f) $\{\delta_{iso}^1, \delta_{iso}^2\} = \{10, 0\}$ ppm. The quadrupolar tensor orientations were $\Omega_Q^1 = (0, 40^\circ, 0)$; $\Omega_Q^2 = (0, 75^\circ, 60^\circ)$, except in (e and f) that used parallel tensors: $\Omega_Q^1 = \Omega_Q^2 = (0, 0, 0)$.

2Q-dimension is reduced. (ii) Spinning sidebands from anisotropic interactions do no longer appear folded exactly at the center-peaks. An interaction-scaling factor of 0.7 ($k = 0.15$) was used to record the data of Fig. 6(d). Despite this precaution, the spectral window of $\omega_r/2\pi = 16.5$ kHz was not sufficiently large to prevent folding of some $2Q_{CT}(AlO_6\text{-}AlO_6)$ signals.

4. Signal sensitivity and 2D peak amplitudes

4.1. 1Q–1Q[2QF] and 2Q–1Q correlations

A 2QF process unavoidably gives signal losses from powders. The transfer efficiency from a source density operator ρ_S to a target ensemble state ρ_T through $2Q_{CT}$ is given by a transfer function $f_{\rho_S\to\rho_T}^{2QF}$, defined formally as $f_{\rho_S\to\rho_T}^{2QF} = \mathrm{Tr}\{\rho_S\rho_T\}/\mathrm{Tr}\{\rho_S^2\}$, where Tr{…} denote the trace operation. We refer to Ref. [17] for further details. Throughout, we neither indicate the dependence of $f_{\rho_S\to\rho_T}^{2QF}$ on τ_{exc} and τ_{rec}, nor on the spatial orientation of the crystallite.

Assuming an ensemble of spin-pairs prepared with equal longitudinal CT polarizations of the two spins, $\rho_S = S_z^{CT} = S_{jz}^{CT} + S_{kz}^{CT}$, the efficiency of the transfer $S_z^{CT} \overset{2QF_{CT}}{\to} S_z^{CT}$ is

$$f_{Z\to Z}^{2QF} = \frac{\mathrm{Tr}\left\{S_z^{CT} V S_z^{CT} V^\dagger\right\}}{\mathrm{Tr}\left\{S_z^{CT} S_z^{CT}\right\}}, \tag{1}$$

where the operator V accounts for the excitation and filtering through $2Q_{CT}$. For two coupled spins-1/2 in a powder, the 2Q-recoupling techniques employed herein offers a theoretical optimum 2QF efficiency of 52% [10,12]. However, for $2QF_{CT}$ of half-integer spin-pairs, the experimental efficiencies are in practice much lower, typically $f_{Z\to Z}^{2QF} < 0.1$ for $S = 3/2$ and $f_{Z\to Z}^{2QF} < 0.05$ for $S = 5/2$ [3,8]. Equal transfer efficiencies result for each spin j and k, $f_{Z\to jz}^{2QF} = f_{Z\to kz}^{2QF}$, as well

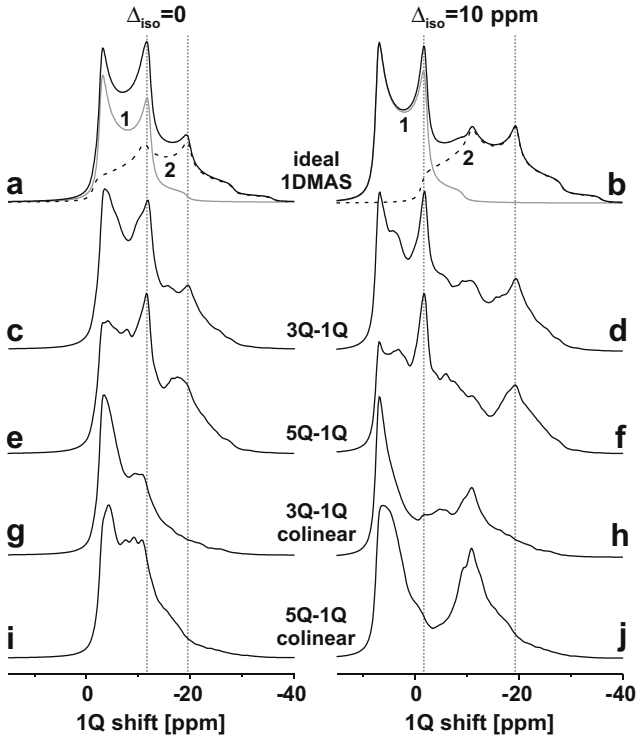

Fig. 5. Calculated NMR spectra for the $S = 5/2$ systems of Fig. 4 with $\{\delta^1_{iso}, \delta^2_{iso}\} = \{0, 0\}$ ppm (left panel) and $\{\delta^1_{iso}, \delta^2_{iso}\} = \{10, 0\}$ ppm (right panel). (a, b) Ideal $1Q_{CT}$ NMR spectra with component peaks of sites **1** and **2** displayed by gray and dashed traces, respectively. (c–j) ω_2-projections of the respective MQ–1Q[2QF] spectra shown in Fig. 4 with non-coinciding (c–f) and aligned (g–j) quadrupolar tensors. Dashed lines mark the right singularity of each second-order quadrupolar-broadened peakshape.

as between any source spin and target spin, i.e., $S^{CT}_{pz} \overset{2QF_{CT}}{\rightarrow} S^{CT}_{qz}$ $(p, q = j, k)$ [16,18,40]:

$$f^{2QF}_{jz\rightarrow jz} = f^{2QF}_{jz\rightarrow kz} = f^{2QF}_{kz\rightarrow jz} = f^{2QF}_{kz\rightarrow kz} = 2f^{2QF}_{Z\rightarrow jz} = 2f^{2QF}_{Z\rightarrow kz} = f^{2QF}_{Z\rightarrow Z} \tag{2}$$

Eqs. (2) have the following practical consequences: (i) In the 1Q–1Q[2QF] NMR spectrum, four equally intense peaks appear [16,18]. (ii) The $2Q_{CT}(j-k)$ coherence signals appearing in the 2Q–1Q spectrum at the ω_2-frequencies ω_j and ω_k are associated with equal integrals $\left(f^{2QF}_{Z\rightarrow jz} = f^{2QF}_{Z\rightarrow kz}\right)$.

4.2. MQ–1Q[2QF] correlations

When assessing the 2D NMR amplitudes from a MQ–1Q[2QF] correlation experiment, it is necessary to account for a non-uniform distribution of longitudinal CT-polarization between the two spins of each pair, since the (single-spin) MQF efficiency $\left(f^{MQF}_{jz\rightarrow jz}\right)$ of a given quadrupolar site depends on its associated quadrupolar interaction-strength and generally diminishes for increasing value of C_Q [25,28]. In Fig. 7(a) for instance, the integrated 3QF signal from site **2** is only 68% of that from site **1**, as opposed to the simulated 2D spectrum of (b) that assumed perfect $Z \rightarrow 3Q$ and $3Q \rightarrow Z$ transfers (compare the ω_1 projections of the 2D spectra). Further, alterations in the line*shapes* may be observed [31,32,36]. However, the projections of Fig. 7(a, b) reveal very similar peakshapes. Hence, (here) the gross consequence of the 3QF stage is a scaling of the NMR signal from each quadrupolar site, depending on its associated C_Q-value. On the other hand, distortions are clearly visible around the regions of the left spectral singularities stemming from *both* quadrupolar sites in the 5Q–1Q[2QF] spectra [compare the ω_2-projections in Fig. 5(c,d) and (e,f)]. The dependence of the 3QF or 5QF processes on the quadrupolar parameters may be reduced by utilizing various options for driving the coherence transfers [27–37].

For MQ–1Q[2QF] experiments, the overall transfer efficiency $\left(f^{eff}_{Z\rightarrow Z}\right)$ of the schematic process

$$S_{jz} + S_{kz} \overset{MQF}{\rightarrow} f^{MQF}_{jz\rightarrow jz} S^{CT}_{jz} + f^{MQF}_{kz\rightarrow kz} S^{CT}_{kz} \overset{2QF_{CT}}{\rightarrow} f^{eff}_{Z\rightarrow Z}\left(S^{CT}_{jz} + S^{CT}_{kz}\right) \tag{3}$$

needs to be considered. It starts from total longitudinal polarization of both spins, which is first transferred to longitudinal CT polarization and subsequently filtered through $2Q_{CT}$. This gives

$$f^{eff}_{Z\rightarrow Z} = \frac{1}{2}\left(f^{MQF}_{jz\rightarrow jz} + f^{MQF}_{kz\rightarrow kz}\right) f^{2QF}_{Z\rightarrow Z}, \tag{4}$$

with $f^{2QF}_{Z\rightarrow Z}$ given by Eq. (1). The combination of two subsequent MQF-processes provides a net transfer efficiency given by a product of two (small) numbers $f^{MQF}_{pz\rightarrow pz}$ and $f^{2QF}_{Z\rightarrow Z}$. Often, this results in very poor *S/N* in MQ–1Q[2QF] NMR experiments and constitutes a major practical limitation. For instance, a 3Q–1Q[2QF] spectrum recorded from sillimanite (not shown) did not permit unambiguous detection of the cross-peaks. On the other hand, Na_2SO_3 (Fig. 2) represents a favorable case where both MQF stages are relatively efficient, as discussed in the SI.

We now consider the 2D peak amplitude a_{pq} in a MQ–1Q[2QF] NMR spectrum, i.e., the peak stemming from MQC evolution during t_1 of spin p combined with $1Q_{CT}$ evolution of spin q during t_2. It appears at a 2D coordinate ω_{pq}, with $p, q = j, k$ and

$$\begin{aligned} a_{jj} = a_{jk} &\sim \frac{1}{4} f^{MQF}_{jz\rightarrow jz} f^{2QF}_{Z\rightarrow Z} \\ a_{kj} = a_{kk} &\sim \frac{1}{4} f^{MQF}_{kz\rightarrow kz} f^{2QF}_{Z\rightarrow Z} \end{aligned} \tag{5}$$

Hence, despite that initially $f^{MQF}_{jz\rightarrow jz} \neq f^{MQF}_{kz\rightarrow kz}$, the signal intensities of the two spins j and k passing through the $2Q_{CT}$ filter become equalized; the ω_2-projection of the 2D spectrum comprises two components with integrals $(a_{jj} + a_{kj}) = (a_{jk} + a_{kk}) = f^{eff}_{Z\rightarrow Z}/2$ [see Eqs. (4) and (5)]. However, the integrals of the two cross-peaks are generally *not* equal $(a_{jk} \neq a_{kj})$, as each is weighted by its respective single-spin MQF efficiency, $f^{MQF}_{jz\rightarrow jz}$ or $f^{MQF}_{kz\rightarrow kz}$. The integral of the auto-correlation signal at ω_{jj} is equal to that of its cross-peak at the frequency ω_{jk}, but distinct from that at ω_{kj} [Eq. (5)]. All these features are verified by the 2D spectrum of Fig. 7(c). It was obtained using an "idealized" $2QF_{CT}$ process that phenomenologically arranged a uniform filtering efficiency for all crystal orientations in the powder, but emulated the distinct 3QF efficiencies of sites **1** and **2** by using initial site populations of 0.595:0.405. Note that the ω_2-projection of Fig. 7(c) agrees well with both of (a) and (b), while its ω_1-projection reproduces the corresponding numerically exact result in (a).

The discussion of peak amplitudes thus far ignored potential $2QF_{CT}$ contributions from equivalent spins. The frequency position of the $2Q_{CT}(j-j)$ peak coincides with the "diagonal" signal-portion of the $2Q_{CT}(j-k)$ correlation. These 2D peaks superimpose to a net integral of $a^{jj}_{jj} + a^{jk}_{jj}$ at the coordinate ω_{jj} (superscripts label the respective spin-pairs).

5. Double-quantum excitation dependence on tensor orientations

An intrinsic feature of MQF processes is their tendency to distort MQF $1Q_{CT}$ NMR powder peak-shapes due to the dependence on the crystallite (dipolar vector) orientation relative to the magnetic field direction. The $2FQ_{CT}$ stage generally induces a strong peak-shape dependence on the relative orientations between pairs of quadrupolar/quadrupolar as well as dipolar/quadrupolar tensors [15,43]. This is manifested by the 2D correlation spectra of Fig. 4(c,d) and (e,f), whose underlying spin parameters only differ

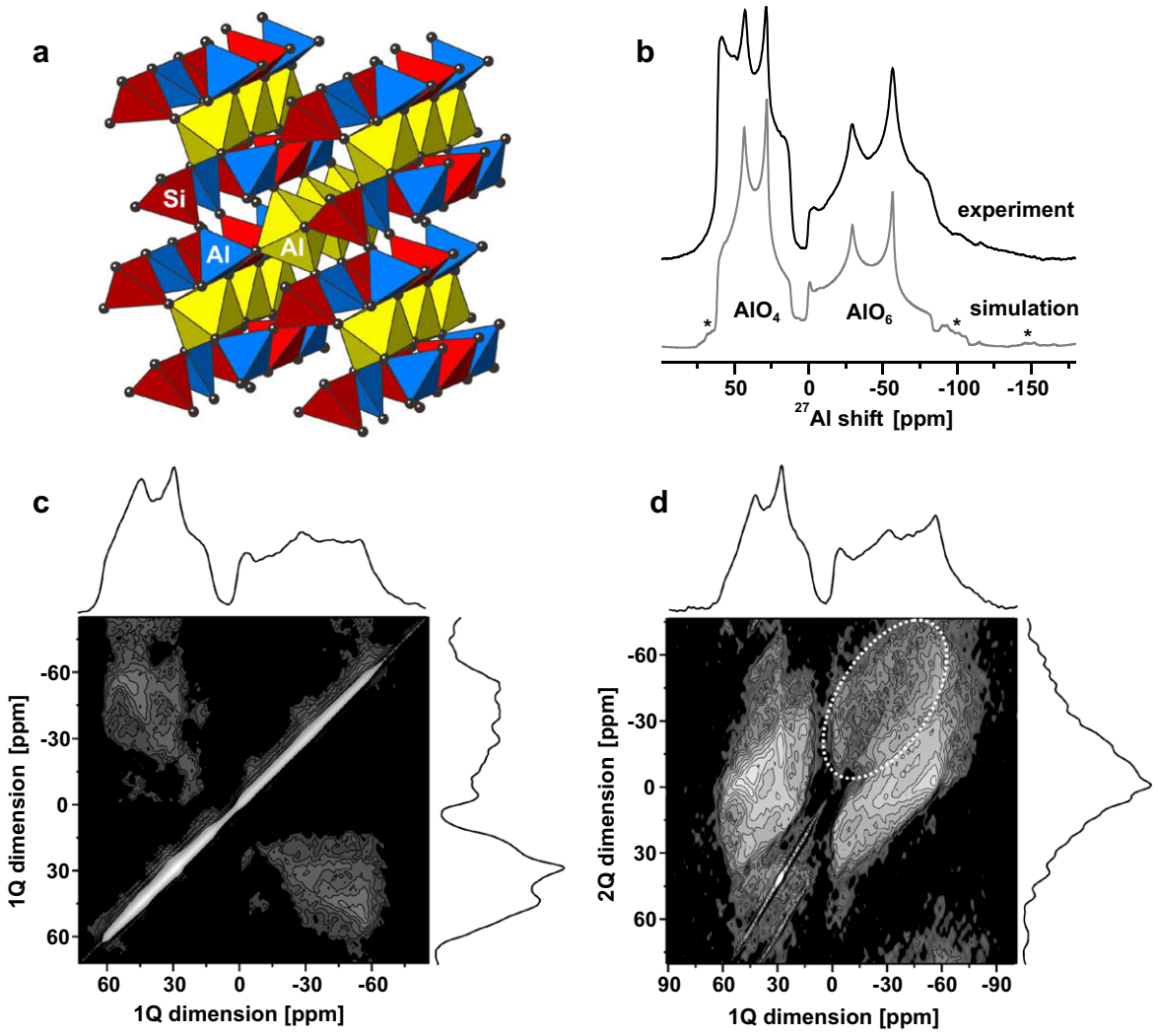

Fig. 6. (a) Structure of sillimanite, $SiAl_2O_5$, with SiO_4 and AlO_4 tetrahedra displayed in red and blue color, respectively. (b) Experimental and simulated ^{27}Al MAS NMR spectra at 9.4 T and $\omega_r/2\pi = 16.5$ kHz. Asterisks mark positions of spinning sidebands. (c) 1Q–1Q[2QF] and (d) 2Q–1Q[2QF] correlation NMR spectra with accompanying projections. A shift-scaling of 0.7 was implemented along the 2Q-dimension, giving an auto-correlation ridge with slope 1.4 ($\delta_1 = 1.4\delta_2$). Yet, some signals appear folded from top to bottom in (d). (For interpretation of the references to color in this figure legend, the reader is referred to the web version of this paper.)

in the relative orientations of the dipolar and quadrupolar tensors. The spectra of (e) and (f) were generated using coincident directions of both quadrupolar tensors and the **1**–**2** dipolar vector. This scenario strongly attenuates the right singularity ("horn") of each second-order quadrupolar-broadened powder pattern, which is clearly manifested by the ω_2-projections shown in Fig. 5 [e.g., compare (c) with (g) and (f) with (j)]. In Fig. 2, the diminished intensity at the right spectral portion of the Na**1**–Na**2** cross-peak also signifies coinciding quadrupolar and dipolar vectors [43].

Experimental peakshapes may only be faithfully reproduced by numerical simulations that explicitly account for the dipolar recoupling process, as demonstrated in our previous analysis of 2Q–1Q correlations [43]. This is evidenced from the 2D spectra of Figs. 7(c) and 8(a): whereas the relative 2D peak *integrals* are in excellent agreement (see Section 4.2), the peak*shape-features* differ substantially. Those of the numerically exact spectrum of Fig. 8(a) are distorted when using coincident interaction tensors. Fig. 8 explores the cross-peak-dependence further when varying the dipolar vector direction but keeping fixed (and parallel) quadrupolar tensors.

The $2QF_{CT}$-altered peak-shapes allow determinations of the absolute quadrupolar tensor orientations (in the crystal frame) by using $2QF_{CT}$ techniques coupled with exact numerical simulations [43]. This constitutes one advantage of using 2Q–1Q or MQ–1Q[2QF] correlation protocols compared to those relying on magnetization transfers over long intervals, as in Refs. [19–22]. However, this favorable feature is currently plagued by two major practical obstacles: (i) Due to the inherently low signal sensitivity following application of $2QF_{CT}$, particularly so for MQ–1Q[2QF] experiments that involves an additional MQF event, long *experimental* acquisition times are required to achieve reasonable *S/N* for accurate tensor-orientation analyses. (ii) The numerically exact 2D spectral *simulations* are extremely time-consuming, which limits the orientational space of tensor orientations that may realistically be explored by currently available standard computer resources. Accurate analyses of coupled $S = 5/2$ appear at present to be out of reach. Both experimental and numerical obstacles are anticipated to be alleviated by future methodological advances.

Considering (i) and (ii), we recommend to (1) first estimate the *relative* orientations between the *quadrupolar* tensors based on an experimental 2D spectrum obtained from any of the techniques in Refs. [19–23] that employ long mixing intervals, thereby allowing for rapid spectral simulations by omitting the dipolar recoupling stage. (2) Whenever experimental S/N permits, a subsequent

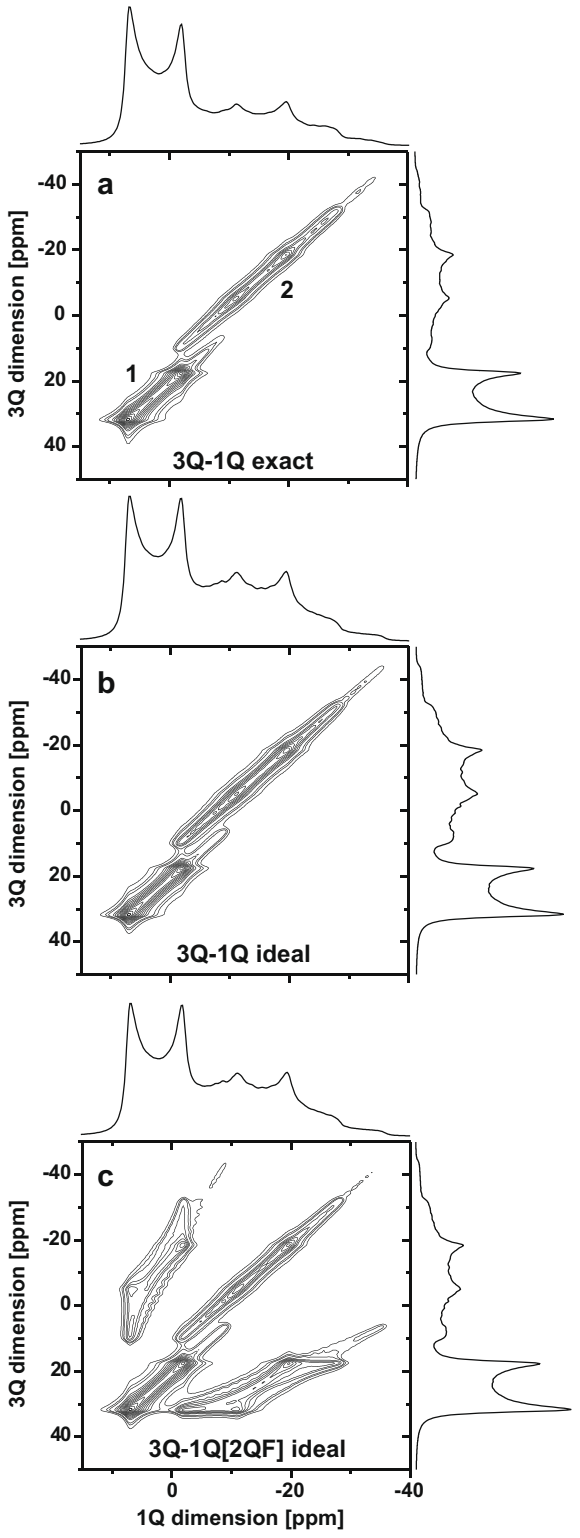

Fig. 7. (a,b) Calculated 3Q–1Q 2D spectra for the NMR parameters and conditions of Fig. 4(e). The simulations only differ in their handling of the 3QF stage, i.e., (a) using a numerically exact calculation or (b) phenomenologically arranging an ideal and orientation-independent 3QF process. Note the very similar powder peakshapes in (a,b); however, due to the dependence of the 3QF on the quadrupolar coupling constants in (a), the integrated signal from spin **2** is only 68% of that for spin **1**. (c) Simulated 3Q–1Q[2QF] NMR spectrum, assuming ideal 3QF as well as $2QF_{CT}$ processes but employing initial spin-populations **1:2** of 0.595:0.405. All remaining differences between the NMR spectrum in (c) and that of Fig. 4(e) reflect the orientational dependence of the $2QF_{CT}$ stage in the latter spectrum.

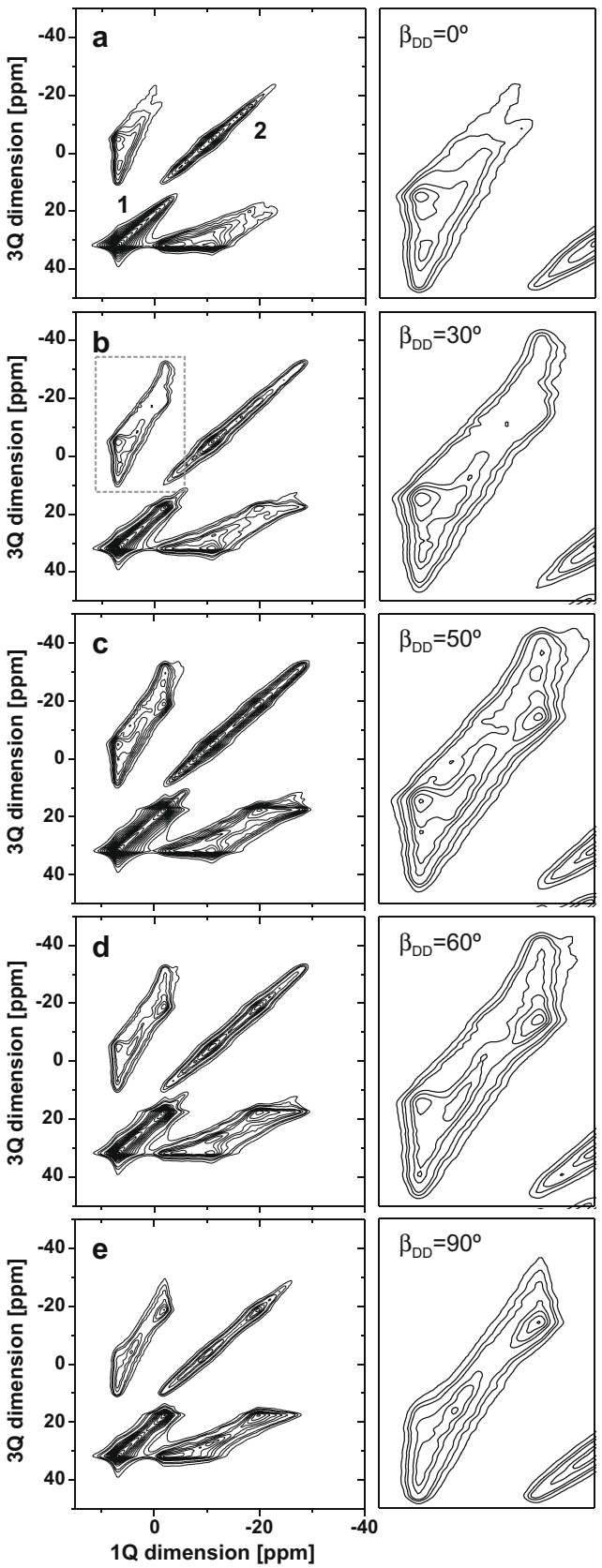

Fig. 8. 3Q–1Q[2QF] spectra simulated using the NMR parameters and conditions of Fig. 4(e) with two coinciding quadrupolar tensors $\Omega_Q^1 = \Omega_Q^2 = (0, 0, 0)$, but varying the Euler angle β_{DD}^{12} of the dipolar vector as follows: (a) 0; (b) 30°; (c) 50°; (d) 60°; (e) 90°. The right panel displays zoomed regions around each left cross-peak (marked by the box in (b)).

analysis of 2Q–1Q, 1Q–1Q[2QF] or MQ–1Q[2QF] spectra is pursued to fixate the quadrupolar tensor orientations by deducing their relative dipolar vector direction, parametrized by Ω_{DD}^{jk} and restricted to two fitting parameters $\left(\beta_{DD}^{jk}, \gamma_{DD}^{jk}\right)$.

6. Materials and methods

6.1. Experimental

Experiments were performed at 9.4 T using a Varian/Chemagnetics Infinity-400 spectrometer and full 4 mm zirconia rotors. All experiments and simulations used hard pulses at an rf nutation frequency $|\gamma_S|B_1/2\pi = 110$ kHz for (single-spin) MQF processes [25–27]. ^{23}Na and ^{27}Al chemical shifts are given relative to Na-Cl(aq) and $Al(NO_3)_3$(aq), respectively. Hypercomplex processing [40] was employed in all 2D experiments and simulations. NMR spectra were normalized to unity maximum 1D or 2D amplitude (except for Fig. 7).

The 3Q–1Q and 3Q–1Q[2QF] acquisitions of Na_2SO_3 were carried out under identical experimental conditions at $\omega_r/2\pi = 12.0$ kHz. $2QF_{CT}$ used $R2_2^1R2_2^{-1}$ for $\tau_{exc} = \tau_{rec} = 667$ μs. 3QC excitation and reconversion pulses were 5.2 μs and 2.0 μs, respectively, whereas CT-selective $\pi/2$ and π pulses operated at $\omega_{nut}^{CT}/2\pi = 6.6$ kHz. The 3Q–1Q[2QF] acquisition resulted from 384 accumulated signal transients for each of 76 t_1-increments, using 1.5 s relaxation delays, $\Delta t_1 = \Delta t_2 = \tau_Z = \tau_r$ and $N = 4$ (see Fig. 1). Total acquisition time: 24 h. The (t_1, t_2) data-set was zero-filled to (512×2048) points and apodized by 50 Hz Gaussian broadening in the t_1-dimension. The lowest contour levels of Fig. 2 are set at 2% of the maximum 2D amplitude.

The natural sillimanite sample (Brandywine Springs, Delaware, USA; catalog number NRM #18770189) was kindly provided and characterized by Ulf Hålenius at the Swedish Museum of Natural History. The phase purity and composition was verified by X-ray powder diffraction and electron microprobe analysis, respectively. Excellent agreement was found between nominal and analyzed ($Si_{1.00}Al_{2.00}O_{5.00}$) compositions. The 2Q–1Q and 1Q–1Q[2QF] ^{27}Al NMR acquisitions at $\omega_r/2\pi = 16.5$ kHz used identical rf-pulse parameters. Inversion and $\pi/2$ pulses operated at $\omega_{nut}^{CT}/2\pi = 22$ kHz; $2QF_{CT}$ employed one completed $R2_4^1R2_4^{-1}$ cycle for $\tau_{exc} = \tau_{rec} = 485$ μs with $N = 2$ and $\delta_{carrier} = -15$ ppm. 26 pairs of RAPT/FAM pulses [30,46] was used prior to the acquisitions of all ^{27}Al 1D, 2Q–1Q and 1Q–1Q[2QF] MAS experiments ($|\gamma_S|B_1/2\pi \approx 110$ kHz; $\tau_p = 0.7$ μs; CT-signal enhancement factor 2.2). Both 2D acquisitions used $\Delta t_1 = \tau_Z = 60.61$ μs and $\Delta t_2 = 15.15$ μs with 1 s relaxation delays. Signal apodization employed Lorentzian (along t_1) and shifted Lorentzian (along t_2) decays of 150 Hz (for 2Q–1Q data) and 200 Hz (for 1Q–1Q[2QF]). Specific for 1Q–1Q[2QF] experiment: 2048 transients/t_1-value; acquired data-size (62×330), zero-filled to (256×1024); total experimental time: 71 h. Specific for 2Q–1Q acquisition: 1280 transients/t_1-value; acquired data-size (32×280), zero-filled to (128×1024); total experimental time: 23 h. The intensity plots of Fig. 6 employed a logarithmic intensity incrementation from the lowest levels of 0.75% (c) and 2.5% (d) of the maximum 2D amplitude. Some levels are contoured for easier visualization.

6.2. Numerical simulations

1D and 2D NMR spectral calculations employed small-step (<1 μs) integration of the Schrödinger equation [47] during t_1 and t_2 evolutions, as well as $2QF_{CT}$ and MQF events (see exceptions below). The simulations accounted for isotropic chemical shifts, dipolar, first- and second-order quadrupolar interactions of the given spin-pairs and rf sequences, except that (i) the CT-selective π-pulse (Fig. 1) was not considered and (ii) the $\pi/2$-pulses bracketing the 2Q-recoupling blocks were implemented as ideal CT-selective pulses. These simplifications, combined with rotor-synchronized t_1-sampling in all 2D simulations, allowed for a full exploitation of the time-periodicity of the spin Hamiltonian to minimize the number of explicitly integrated time-segments [47]. The initial density operator was S_z for calculations of MQ–1Q[2QF] spectra and S_z^{CT} for those of 2Q–1Q and 1Q–1Q[2QF] schemes. The CT-part of the S^+ operator was detected, using the COMPUTE algorithm for optimal speed [48]. MQF events were implemented by nulling all density matrix elements but those of the relevant coherence order.

All MQ–1Q-based simulations arranged correlations of the coherence orders $\{-|M|\leftrightarrow -1\}$. Between 160 and 200 t_1-increments were explicitly calculated (zero-filled to 512 or 1024 points) with 100–150 Hz Lorentzian apodization applied along each spectral dimension. The results in Fig. 2(c) was obtained from the summation of 25 individual 2D spectra (see Ref. [43]). $R2_4^1R2_4^{-1}$ with $\tau_{exc} = \tau_{rec} = 800$ μs was used for 2Q-recoupling in all simulations, except that of Fig. 2(c). The single-spin MQF utilized hard pulses as follows: $\{\tau_{exc}, \tau_{rec}\} = \{5.2, 2.5\}$ μs for 3QF of $S = 3/2$; $\{\tau_{exc}, \tau_{rec}\} = \{3.6, 1.2\}$ μs for 3QF and {4.0, 2.0} μs for 5QF of $S = 5/2$, respectively. The rf carrier frequency was set at 0 ppm throughout, except during t_1-evolution of the 5Q–1Q[2QF] simulations in Fig. 4 ($\delta_{carrier} = 14.38$ ppm). All other conditions and parameters are listed in the figure captions.

Powder averaging was performed over 6044 three-angle ZCW orientations [49,50], except for the 3Q–1Q[2QF] simulation of Na_2SO_3 (3722 orientations). The calculations of 1D MAS spectra and the idealized 3Q–1Q-based spectra in Fig. 7(b, c) employed a two-angle ^{ROSE}LEBh6535 set [51]. On a 3.0 GHz Intel Core CPU personal computer, a MQ–1Q[2QF] simulation typically lasted for ≈ 1 h for pairs of $S = 3/2$ (Figs. 3 and S1) and for 12 h for $S = 5/2$ pairs (Figs. 4 and 8).

7. Concluding remarks

We have compared 1Q–1Q[2QF], MQ–1Q[2QF] and 2Q–1Q correlation schemes for probing homonuclear quadrupolar spin-pairs. Thanks to its combination of best signal sensitivity (which is, however, essentially paralleled by the 1Q–1Q[2QF] experiment) and outstanding capabilities for detecting correlations between equivalent spins, the 2Q–1Q protocol [14,15] shows promise to remain as the best general-purpose experimental technique for establishing internuclear proximities. However, its main problem compared to the other correlation protocols is the requirement of using rotor-synchronized t_1-incrementation [45]. While such sampling improves *S/N* by folding of all spinning sidebands onto the centerband [44], the ω_r-limited spectral window is often insufficient to accommodate all second-order broadened $2Q_{CT}$ signals: this necessitates experimentation at high MAS frequencies and the unavoidable need to use small-volume rotors and thereby compromising NMR signal sensitivity.

The numerically simulated spin systems considered herein may be viewed as relatively problematic cases concerning NMR signal separation at $B_0 \lesssim 17$ T. Nevertheless, only scenarios of two coupled spins were considered, whereas often several quadrupolar sites are present in experimentally interesting samples. Strong overlap between two or several 2Q–1Q correlation signals may then give ambiguous peak assignments, particularly around the auto-correlation diagonal region of the 2D NMR spectrum (e.g., see Figs. 4 and 5 of Ref. [8]). Primarily in such cases, the MQ–1Q[2QF] experiments gain value relative to the more sensitive and intrinsically more informative 2Q–1Q acquisitions. Therefore, we anticipate that MQ–1Q[2QF] experimentation will chiefly be

of value to ascertain/preclude the presence of site-connectivities for certain spin-pairs that produce unresolved signals in 2Q–1Q NMR spectra, whereas the 2Q–1Q protocol is likely to constitute the primary engine for determining inter-spin proximities.

The main practical limitation of the MQ–1Q[2QF] experiment is its very poor signal sensitivity, given roughly as the product of the individual filtering efficiencies of $2Q_{CT}$ and MQ coherences. However, here we employed the most straightforward implementations [25–27] for MQ excitation and reconversion. There should be room for improvements [29–36]: particularly, soft-pulse added mixing (SPAM) [37] and quadrupolar Carr–Purcell–Meiboom–Gill (QCPMG) [52] techniques are expected to provide signal enhancements. The latter has already been demonstrated in the context of 2Q–1Q correlations [53]. However, more substantial sensitivity improvements are promised by combining $2QF_{CT}$ with a satellite transition MAS (STMAS) scheme [54–56]. Especially, 2QF-STMAS[2QF]-type implementations are expected to offer artifact-free NMR correlations and a reasonable signal sensitivity [54–56] (only marginally lower than that of a 1Q–1Q[2QF] experiment). The main drawbacks are its stringent demands for accurate magic-angle-setting and MAS stability [54,56].

An option for improving spectral resolution in any of the protocols discussed herein is offered by spectral editing of individual NMR signals by exploiting site-selectivity based on either chemical shifts or quadrupolar coupling constants [57], analogously to previous demonstrations in the context of heteronuclear correlations [58]. We are currently exploring such possibilities for the present homonuclear NMR techniques.

Acknowledgments

This work was supported by the Swedish Research Council (VR), the Carl Trygger Foundation (CTS), the Knut and Alice Wallenberg Foundation (KAW) and the Faculty of Natural Sciences at Stockholm University. I thank Ulf Hålenius for providing and characterizing the sillimanite sample and Baltzar Stevensson for producing the data in Table S1.

Supplementary information

Supplementary text and figures associated with this article can be found, in the online version, at doi:10.1016/j.jmr.2010.02.007.

References

[1] S.E. Ashbrook, M.J. Duer, Structural information from quadrupolar nuclei in solid state NMR, Concepts Magn. Reson. A 28 (2006) 183–248.
[2] J.-P. Amoureux, J. Trébosc, L. Delevoye, O. Lafon, B. Hu, Q. Wang, Correlation NMR spectroscopy involving quadrupolar nuclei, Solid State NMR 35 (2009) 12–18.
[3] M. Edén, Homonuclear dipolar recoupling of half-integer spin quadrupolar nuclei: techniques and applications, Solid State NMR 36 (2009) 1–10.
[4] M. Carravetta, M. Edén, X. Zhao, A. Brinkmann, M.H. Levitt, Symmetry principles for the design of radiofrequency pulse sequences in the nuclear magnetic resonance of rotating solids, Chem. Phys. Lett. 321 (2000) 205–215.
[5] M. Carravetta, M. Edén, O.G. Johannessen, H. Luthman, P.J.E. Verdegem, J. Lugtenburg, A. Sebald, M.H. Levitt, Estimation of carbon–carbon bond lengths and medium-range internuclear distances by solid-state nuclear magnetic resonance, J. Am. Chem. Soc. 123 (2001) 10628–10638.
[6] A. Brinkmann, M.H. Levitt, Symmetry principles in the nuclear magnetic resonance of spinning solids: heteronuclear recoupling by generalized Hartmann–Hahn sequences, J. Chem. Phys. 115 (2001) 357–384.
[7] A. Brinkmann, M. Edén, Second order average Hamiltonian theory of symmetry-based pulse schemes in the nuclear magnetic resonance of rotating solids: application to triple-quantum dipolar recoupling, J. Chem. Phys. 120 (2004) 11726–11744.
[8] M. Edén, D. Zhou, J. Yu, Improved double-quantum NMR correlation spectroscopy of dipolar-coupled quadrupolar spins, Chem. Phys. Lett. 431 (2006) 397–403.
[9] A.Y.H. Lo, M. Edén, Efficient symmetry-based homonuclear dipolar recoupling of quadrupolar spins: double-quantum NMR correlations in amorphous solids, Phys. Chem. Chem. Phys. 10 (2008) 6635–6644.
[10] M. Edén, A.Y.H. Lo, Supercycled symmetry-based double-quantum dipolar recoupling of quadrupolar spins: I. Theory, J. Magn. Reson. 200 (2009) 267–279.
[11] R. Tycko, G. Dabbagh, Double-quantum filtering in magic-angle-spinning NMR spectroscopy: an approach to spectral simplification and molecular structure determination, J. Am. Chem. Soc. 113 (1991) 9444–9448.
[12] N.C. Nielsen, H. Bildsoe, H.J. Jakobsen, M.H. Levitt, Double-quantum homonuclear rotary resonance: efficient dipolar recovery in magic-angle-spinning nuclear magnetic resonance, J. Chem. Phys. 101 (1994) 1805.
[13] A. Brinkmann, M. Edén, M.H. Levitt, Synchronous helical pulse sequences in magic-angle-spinning NMR. Double quantum spectroscopy of recoupled multiple-spin systems, J. Chem. Phys. 112 (2000) 8539–8554.
[14] G. Mali, G. Fink, F. Taulelle, Double-quantum homonuclear correlation magic angle sample spinning nuclear magnetic resonance spectroscopy of dipolar-coupled quadrupolar nuclei, J. Chem. Phys. 120 (2004) 2835–2845.
[15] A.J. Painter, M.J. Duer, Double-quantum-filtered nuclear magnetic resonance spectroscopy applied to quadrupolar nuclei in solids, J. Chem. Phys. 116 (2002) 710–722.
[16] H. Geen, J. Gottwald, R. Graf, I. Schnell, H.W. Spiess, J.J. Titman, Elucidation of dipolar coupling networks under magic-angle-spinning, J. Magn. Reson. 125 (1997) 224–227.
[17] M. Edén, A. Brinkmann, Triple-quantum dynamics in multiple-spin systems undergoing magic-angle spinning: application to ^{13}C homonuclear correlation spectroscopy, J. Magn. Reson. 173 (2005) 259–279.
[18] A.S.D. Heindrichs, H. Geen, J.J. Titman, MAS double-quantum filtered dipolar shift correlation spectroscopy, J. Magn. Reson. 147 (2000) 68–77.
[19] N.G. Dowell, S.E. Ashbrook, J. McManus, S. Wimperis, Relative orientation of quadrupole tensors from two-dimensional multiple-quantum MAS NMR, J. Am. Chem. Soc. 123 (2001) 8135–8136.
[20] N.G. Dowell, S.E. Ashbrook, S. Wimperis, Relative orientation of quadrupole tensors from high-resolution NMR of powdered solids, J. Phys. Chem. A 106 (2002) 9470–9481.
[21] M. Edén, J. Grinshtein, L. Frydman, High resolution 3D exchange NMR spectroscopy and the mapping of connectivities between half-integer quadrupolar nuclei, J. Am. Chem. Soc. 124 (2002) 9708–9709.
[22] M. Edén, L. Frydman, Homonuclear NMR correlations between half-integer quadrupolar nuclei undergoing magic-angle spinning, J. Phys. Chem. B 107 (2003) 14598–14611.
[23] M. Edén, H. Annersten, Å. Zazzi, Pulse-assisted homonuclear dipolar recoupling of half-integer quadrupolar spins in magic-angle spinning NMR, Chem. Phys. Lett. 410 (2005) 24–30.
[24] L. Frydman, J.S. Harwood, Isotropic spectra of half-integer quadrupolar spins from bidimensional magic-angle-spinning NMR, J. Am. Chem. Soc. 117 (1995) 5367–5368.
[25] A. Medek, J.S. Harwood, L. Frydman, Multiple-quantum magic-angle-spinning NMR: a new method for the study of quadrupolar nuclei in solids, J. Am. Chem. Soc. 117 (1995) 12779–12787.
[26] C. Fernandez, J.-P. Amoureux, 2D-multiquantum MAS-NMR spectroscopy of ^{27}Al in aluminophosphate molecular sieves, Chem. Phys. Lett. 242 (1995) 449–454.
[27] G. Wu, D. Rovnyak, B.Q. Sun, R.G. Griffin, High-resolution multiple-quantum MAS NMR spectroscopy of half-integer quadrupolar nuclei, Chem. Phys. Lett. 249 (1996) 210–217.
[28] J.-P. Amoureux, C. Fernandez, L. Frydman, Optimized multiple-quantum magic-angle-spinning NMR experiments on half-integer quadrupoles, Chem. Phys. Lett. 259 (1996) 347–355.
[29] G. Wu, D. Rovnyak, B.Q. Sun, R.G. Griffin, Quantitative multiple-quantum magic-angle-spinning NMR spectroscopy of quadrupolar nuclei in solids, J. Am. Chem. Soc. 118 (1996) 9326–9332.
[30] P.K. Madhu, A. Goldbourt, L. Frydman, S. Vega, Sensitivity enhancement of the MQMAS NMR experiment by fast amplitude modulation of the pulses, Chem. Phys. Lett. 307 (1999) 41–47.
[31] A.P.M. Kentgens, R. Verhagen, Advantages of double frequency sweeps in static, MAS and MQMAS NMR of spin $I = 3/2$ nuclei, Chem. Phys. Lett. 300 (1999) 435–443.
[32] T. Vosegaard, P. Florian, D. Massiot, P.J. Grandinetti, Multiple quantum magic-angle spinning using rotary resonance excitation, J. Chem. Phys. 114 (2001) 4618–4624.
[33] H-T. Kwak, S. Prasad, Z. Yao, P.J. Grandinetti, L. Emsley, Enhanced sensitivity in RIACT/MQ-MAS NMR experiments using rotor assisted population transfer, J. Magn. Reson. 150 (2001) 71–80.
[34] K.H. Lim, T. Charpentier, A. Pines, Efficient triple-quantum excitation in modified RIACT MQMAS NMR for $I = 3/2$ nuclei, J. Magn. Reson. 154 (2002) 196–204.
[35] A. Goldbourt, S. Vega, Signal enhancement in 5QMAS spectra of spin-5/2 quadrupolar nuclei, J. Magn. Reson. 154 (2002) 280–286.
[36] P.K. Madhu, M.H. Levitt, Signal enhancement in the triple-quantum magic-angle spinning NMR of spins-3/2 in solids: the FAM-RIACT-FAM sequence, J. Magn. Reson. 155 (2002) 150–155.
[37] Z. Gan, H.T. Kwak, Enhancing MQMAS sensitivity using signals from multiple coherence transfer pathways, J. Magn. Reson. 168 (2004) 346–351.
[38] S.P. Brown, S.J. Heyes, S. Wimperis, Two-dimensional MAS multiple-quantum NMR of quadrupolar nuclei. Removal of inhomogeneous second-order broadening, J. Magn. Reson. A 119 (1996) 280–284.
[39] J.-P. Amoureux, C. Fernandez, S. Steurnagel, Z-filtering in MQMAS NMR, J. Magn. Reson. A 123 (1996) 116–118.

[40] R.R. Ernst, G. Bodenhausen, A. Wokaun, Principles of Nuclear Magnetic Resonance in One and Two Dimensions, Clarendon Press, Oxford, 1987.
[41] D.A. Varshalovich, A.N. Moskalev, V.K. Khersonskii, Quantum Theory of Angular Momentum, World Scientific, Singapore, 1988.
[42] W.P. Power, High-resolution solid-state ^{23}Na NMR of anhydrous sodium sulphite, Magn. Reson. Chem. 33 (1995) 220–223.
[43] M. Edén, Determination of absolute quadrupolar tensor orientations by double-quantum NMR on powders, Chem. Phys. Lett. 470 (2009) 318–324.
[44] D. Massiot, Sensitivity and lineshape improvements of MQ-MAS by rotor-synchronized data acquisition, J. Magn. Reson. A 122 (1996) 240–244.
[45] H. Geen, J.J. Titman, J. Gottwald, H.W. Spiess, Spinning sidebands in the fast-MAS multiple-quantum spectra of protons in solids, J. Magn. Reson. A 114 (1995) 264–267.
[46] Z. Yao, H-T. Kwak, D. Sakellariou, L. Emsley, P.J. Grandinetti, Sensitivity enhancement of the central transition NMR signal of quadrupolar nuclei under magic-angle spinning, Chem. Phys. Lett. 327 (2000) 85–90.
[47] M. Edén, Computer simulations in solid state NMR: II. Implementations for static and rotating samples, Concepts Magn. Reson. A 18 (2003) 1–23.
[48] M. Edén, Y.K. Lee, M.H. Levitt, Efficient simulation of periodic problems in NMR. Application to decoupling and rotational resonance, J. Magn. Reson. A 120 (1996) 56–71.
[49] H. Conroy, Molecular Schrödinger equation. VIII. A new method for the evaluation of multidimensional integrals, J. Chem. Phys. 47 (1967) 5307–5318.
[50] V.B. Cheng, H.H. Suzukawa, M. Wolfsberg, Investigations of a nonrandom numerical method for multidimensional integration, J. Chem. Phys. 59 (1973) 3992–3999.
[51] B. Stevensson, M. Edén, Efficient orientational averaging by the extension of Lebedev grids via regularized octahedral symmetry expansion, J. Magn. Reson. 181 (2006) 162–176.
[52] F.H. Larsen, H.J. Jakobsen, P.D. Ellis, N.C. Nielsen, QCPMG-MAS NMR of half-integer quadrupolar nuclei, J. Magn. Reson. 131 (1998) 144–147.
[53] G. Mali, V. Kaucic, Enhancing sensitivity or resolution of homonuclear correlation experiment for half-integer quadrupolar nuclei, J. Magn. Reson. 171 (2004) 48–56.
[54] Z. Gan, Isotropic NMR spectra of half-integer quadrupolar nuclei using satellite transitions and magic-angle spinning, J. Am. Chem. Soc. 122 (2000) 3242–3243.
[55] H.-T. Kwak, Z. Gan, Double-quantum filtered STMAS, J. Magn. Reson. 164 (2003) 369–372.
[56] S.E. Ashbrook, S. Wimperis, High-resolution NMR of quadrupolar nuclei in solids: the satellite-transition magic angle spinning (STMAS) experiment, Prog. NMR Spectrosc. 45 (2004) 53–108.
[57] H.-T. Kwak, S. Prasad, T. Clark, P.J. Grandinetti, Selective suppression and excitation of solid-state NMR resonances based on quadrupole coupling constants, J. Magn. Reson. 160 (2003) 107–113.
[58] M. Edén, Quadrupolar coupling selective cross-polarization in solid-state NMR, Phys. Chem. Chem. Phys. 8 (2006) 1994–1999.